

Research Article

Annual Optical Performance of a Solar CPC Photoreactor with Multiple Catalyst Support Configurations by a Multiscale Model

Manuel I. Peña-Cruz ¹, Patricio J. Valades-Pelayo,^{2,3} Camilo A. Arancibia-Bulnes ²,
Carlos A. Pineda-Arellano,¹ Iván Salgado-Tránsito,¹ and Fernando Martell-Chavez¹

¹CONACYT-Centro de Investigaciones en Óptica, A.C., Unidad Aguascalientes, Prol. Constitución 607, Frac. Reserva Loma Bonita, Aguascalientes, Aguascalientes 20200, Mexico

²Instituto de Energías Renovables-Universidad Nacional Autónoma de México, Privada Xochicalco s/n, A.P. 34, Col. Centro, Temixco, Morelos 62580, Mexico

³Depto. de Ingeniería de Procesos e Hidráulica, Universidad Autónoma Metropolitana-Iztapalapa, Av. San Rafael Atlixco No. 186, C.P. 09340, Mexico City, Mexico

Correspondence should be addressed to Manuel I. Peña-Cruz; mipec@cio.mx

Received 25 May 2018; Accepted 14 August 2018; Published 10 October 2018

Academic Editor: K. R. Justin Thomas

Copyright © 2018 Manuel I. Peña-Cruz et al. This is an open access article distributed under the Creative Commons Attribution License, which permits unrestricted use, distribution, and reproduction in any medium, provided the original work is properly cited.

In this work, the seasonal and yearly optical performance of supported catalyst CPC solar photocatalytic reactors has been theoretically analyzed. A detailed model for the optical response of the anatase catalyst films is utilized, based on the characteristic matrix method, together with Monte Carlo ray tracing simulations. The catalyst is supported over glass tubes contained inside a larger glass tube that functions as receiver of the CPC reflector. Arrangements with four, five, and six tubes are considered. Overall, the four-tube scenario presents the worst performance of all, followed by the five-tube case. In general, the six-tube configuration is better. Nevertheless, important differences can be observed depending on the specific arrangement of tubes. The six-tube case surpasses the absorption rate of all the other configurations when the distance between tubes is extended. This configuration exhibits 27% increased yearly energy absorption with respect to the reference case and 47% with respect to the worst case scenario.

1. Introduction

Photocatalysis has been a prolific scientific field due to the attractiveness of its applications. Among these are the degradation of various organic compounds in gases [1] and liquids [2], hydrogen production by water splitting [3], and CO₂ reduction for hydrocarbon fuel production (Sarkar et al., 2016). As this process involves the generation of hydroxyl radicals through a photoinduced electrochemical reaction activated in the UV-Vis range, it is feasible to use solar energy as a renewable energy source, making photocatalysis an eco-friendly technology capable of mitigating environmental water pollution [4] or producing alternative fuels [5].

One of the main technologic challenges faced is the need to increase the efficiency of photocatalytic systems at larger

scales [6]. In this regard, a key step for a suitable implementation on a large scale is a proper modeling strategy that can help in photoreactor design and optimization.

While most of the available literature in photoreactor modeling focuses on suspended photoreactors, their supported counterpart still lacks a unified approach [7]. In this regard, the use of pseudocontinuum approximations [8] or empirical models [9] is a common choice. Nonetheless, while empirical models are unsuitable for scale-up purposes, pseudocontinuum models are only applicable to certain support arrangements, which usually are scale-dependent [10].

In particular, solar photocatalytic reactors [11] are very attractive due to the positive impact of using renewable energy as the source of UV radiation for the reactions. A common configuration uses glass tubes as reactors [12],

which are illuminated by a solar reflector, either to increase radiation intensity, by means of parabolic trough concentrators [13], or to improve the distribution of energy in the tube perimeter, by means of V-trough or CPC reflectors [14–17]. Even a modification of the standard CPC geometry to accommodate for a single flat support for the catalyst inside a tubular reactor has been proposed [18].

Most radiation transfer studies have focused on reactors with suspended catalyst [13, 15, 19, 20]. However, fixed catalyst reactors are also of interest [17]. Manassero et al. [21] have carried out experimental comparison and Monte Carlo modeling of suspended and fixed catalyst photoreactors. Recently, our research group proposed a multiscale approach [7] using different methods at the support and the reactor scale. The methods employed are the characteristic matrix method [22] and the Monte Carlo ray tracing method. This method allows studying the effect of relevant parameters, such as photocatalyst film thickness, support surface location, concentrator geometry, optical properties, and even irradiance conditions, hence giving valuable information on the design of supported photoreactors.

In this paper, the assessment of the year-round optical performance of a supported solar CPC photocatalytic reactor is carried out. This evaluation is achieved by coupling meteorological software and a ray tracing software to generate 3D incoming radiation profiles as input for the multiscale model presented by Valadés-Pelayo et al. [7]. Given that no studies in the literature consider the geometrical arrangement (number and disposition) of the tubes, six different arrays are considered. On this basis, this study identifies the best multitubular support layout which collects more radiative energy throughout the year and points out directions towards the improvement of multitubular support configurations.

2. Methodology

2.1. Ray Tracing on the CPC. Ray tracing simulations of the CPC concentrator were carried out to model its optical behavior at different times of the year. For this purpose, the Tonatiuh ray tracing software [23] was used in this work. Tonatiuh is a freely distributed, open-source code, based on the Monte Carlo method, which has been widely utilized for different applications. Among its attractive features, it allows the use of a scripting tool, which enables continuous simulation for relevant scenarios, as parameters are varied. The CPC geometry is already defined in this software as one of its basic concentrator types (see Figure 1).

The characteristics of the solar source need to be defined prior to the simulations. Solar irradiance data has been obtained from a typical meteorological year (TMY) provided by the commercial software Meteonorm®. This software allows obtaining hourly irradiance values through the year for a particular location, employing numerical algorithms coupled to preexisting data from weather stations. In particular, UVA irradiance values were utilized in this analysis, which correspond to the region of the spectrum where the anatase TiO_2 photocatalyst is active [7]. Four typical days (March 21, June 21, September 21, and December 21) were

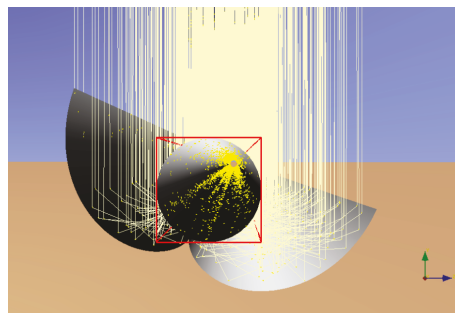


FIGURE 1: CPC under Tonatiuh ray tracing simulation.

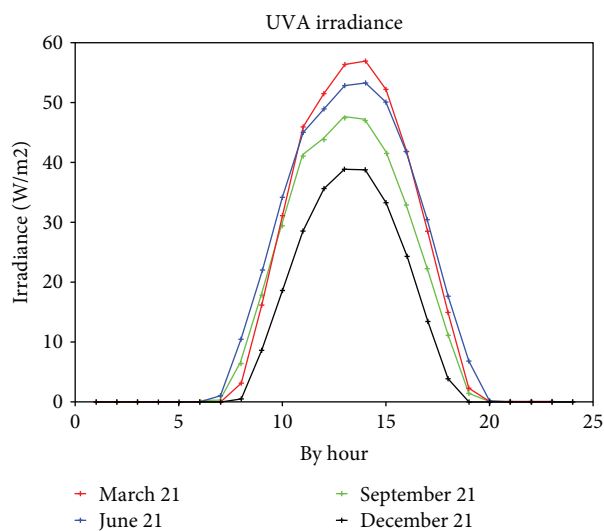


FIGURE 2: Typical UVA irradiance in the city of Aguascalientes, Mexico, as a function of hour, for the solstices and equinoxes.

chosen to present the results (see Figure 2), as they represent best the behavior of the angular position of the sun focusing on the CPC throughout the year. In this case, the local coordinates are defined as $21^{\circ} 52' 52''$ N and $102^{\circ} 17' 29''$ O, corresponding to the city of Aguascalientes, Mexico. We consider this analysis valuable for any particular location. Solar angles may change due to location, but the CPC must be oriented accordingly to the local latitude, providing similar results. UV irradiance may also vary from location to location, but the overall performance of the system must remain, as overall performance is modeled evenly by the amount of UV irradiance reaching the reactor but depends primarily on the geometrical disposition of the tubes for the energy absorption. However, for very high latitudes where winter days are very short, the energetic contribution of this season will be seriously reduced. On the other hand, the static nature of the collector does not allow taking advantage of the much longer summer days. Thus, the yearly energy absorption is reduced.

Commonly, nontracking CPC arrays are tilted to the latitude of the locality under study with the axis of the tubular receiver along the east-west direction, to optimize the yearly

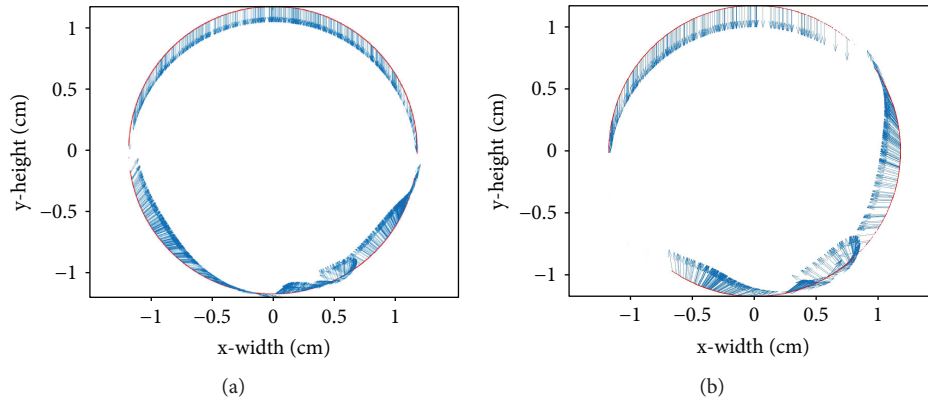


FIGURE 3: Photon vectors impinging on the receiver tube at 13:00 h, for (a) March 21 and (b) December 21.

collection of solar rays. This is also the configuration chosen for the present work.

A script is programmed in order to construct the virtual collector under design specifications, according to Salgado-Trásito et al. [17]. In particular, the outer radius of the glass-tubular receiver is fixed at 1.175 cm. The radii of the inner TiO_2 -coated glass tubes take the values 0.285, 0.342, and 0.4275 cm, according to the number of supporting tubes (6-5-4, respectively), in order to preserve in all cases the same total mass of catalyst inside the reactor. The length of all tubes is 70 cm, and anatase film thickness is fixed at 800 nm. All specular materials of the CPC are considered with ideal reflective properties, in order to evaluate solely the effect of the geometric disposition of the inner tubes in the receiver.

Sun position is calculated accordingly to the particular day and hour of interest. Then, a ray trace simulation with a million rays is performed. This is repeated for every working hour (from 9:00 to 17:00 h). The matrix of photons that reach the external part of the tubular receiver, resulting from these simulations, is stored for further processing by the optical model describing the inner part of the reactor.

The time-dependent solar position vector (S_v) is used as an input for the ray trace simulations

$$S_v = (\cos \gamma_s \sin \theta_z, -\sin \gamma_s \sin \theta_z, \cos \theta_z), \quad (1)$$

where the zenith angle is calculated following Duffie and Beckman ([24]), as

$$\theta_z = \cos^{-1}(\cos \phi \cos \delta \cos \omega + \sin \phi \sin \delta), \quad (2)$$

where ϕ is the site latitude, δ is the solar declination angle, and ω is the hour angle, which varies at a rate of $0.25^\circ/\text{min}$. Similarly, the azimuth angle is calculated as

$$\gamma_s = \text{atan2}(\sin \phi \cos \delta \cos \omega - \cos \phi \sin \delta, \cos \delta \sin \omega), \quad (3)$$

where $\text{atan2}(x, y)$ stands for the two-argument arctangent function, which is able to identify the appropriate quadrant of an angle whose tangent is given by y/x .

The Tonatiuh ray tracer does not deliver directly the photon vectors required in the next step of our simulation on its output file. Instead, it provides the history of collision points of every ray traced. As rays on a CPC can suffer several reflections before reaching the receiver, the direction vectors $\hat{\mathbf{k}}$ must be obtained from the last two impacts of the ray, that with the tube \mathbf{r}_t , and the last reflection on the CPC \mathbf{r}_{lr}

$$\hat{\mathbf{k}} = (\mathbf{r}_t - \mathbf{r}_{lr}) / |\mathbf{r}_t - \mathbf{r}_{lr}|^{-1}. \quad (4)$$

Two plots with excerpts of the photon vectors impinging on the glass-tubular receiver are shown in Figure 3. These vectors are obtained for March 21 and December 21 at 13:00 h. The photon vector map is correlated directly to the day of the year, time, geometry (concentration factor), and tilt of the CPC. As exemplification, the low altitude of the sun on December 21 solstice (Figure 3(b)) produces an irregular distribution of photons, as compared to March 21 equinox (Figure 3(a)).

Ray vector maps such as the above are calculated for every working hour of the chosen days and are passed to the next step of the simulation, which considers propagation inside the receiver tube. A flowchart of the entire optical performance analysis has been resumed in Figure 4.

2.2. Radiation Absorption Model. The methodology allows modeling a number of important design parameters, such as incoming photon's trajectories, reactor geometry, photocatalyst layer thickness, and arrangement of the inner tubes. Key information required for the simulation radiation absorption inside the reactor, is the optical response of the absorber tubes, given in terms of their reflectance, transmittance, and absorptance coefficients. For the anatase film covering the absorber tubes, the characteristic matrix method (CMM) is used.

The CMM allows obtaining the optical response of thin film multilayers based on an electromagnetic description [22]. The application of this theory to glass-supported anatase films has been described in a previous publication [7], and only a brief description is presented here. The reflectance

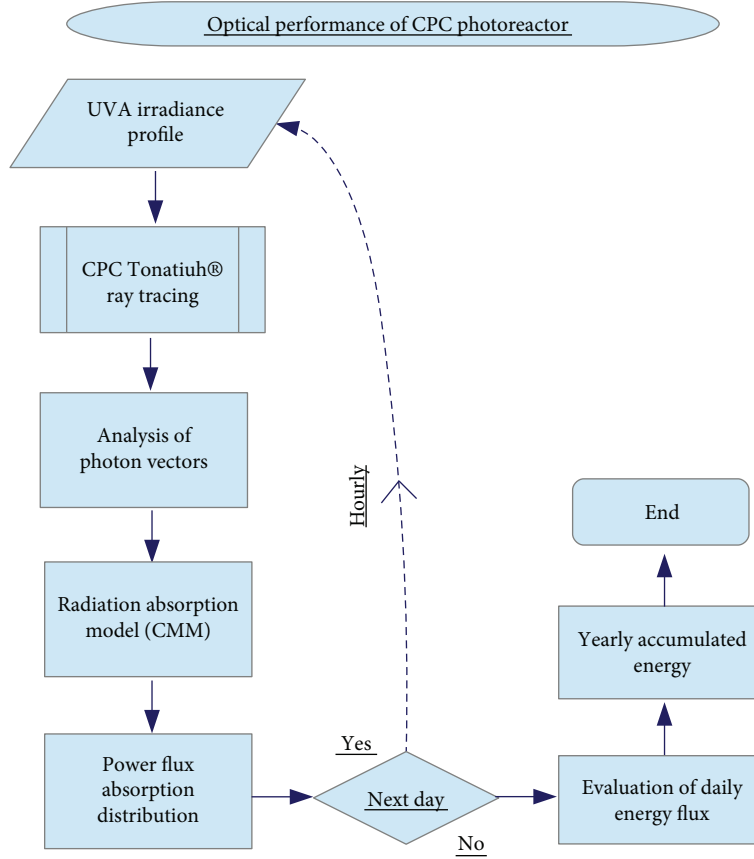


FIGURE 4: Flowchart: optical performance analysis for a CPC photoreactor.

R , transmittance T , and absorptance A of the films covering the tubes are expressed as

$$R = \frac{\left| \left(m'_{11} + m'_{12} p_f \right) p_0 - \left(m'_{21} + m'_{22} p_f \right) \right|^2}{\left| \left(m'_{11} + m'_{12} p_f \right) p_0 + \left(m'_{21} + m'_{22} p_f \right) \right|^2}, \quad (5)$$

$$T = \frac{2p_0}{\left| \left(m'_{11} + m'_{12} p_f \right) p_0 + \left(m'_{21} + m'_{22} p_f \right) \right|^2},$$

$$A = 1 - R - T,$$

where the components of the characteristic matrix m'_{ij} and the coefficients p_0 and p_f depend all on the optical properties of the media involved [7]. The refractive index of glass has been obtained from Rubin [25], the optical properties of the TiO_2 film have been obtained following Viseu et al. (2001), and a value of 1.33 has been considered for the refractive index of water.

For a single interface, for instance, glass/water or glass/air, the above equations reduce to Fresnel formulae [24] for reflection and transmission of radiation. This is the model applied to determine the properties of the receiver tube that encloses the reaction space where the absorber tubes are contained.

Once the involved optical coefficients have been obtained, the next step is to consider the propagation of each of these rays inside the reactor volume by a Monte Carlo method. For this, the set of ray incident in the outer part of the glass receiver tube (described in the previous section) is used. The core part of this process is the determination of all possible collisions of the ray with the different surfaces contained in the volume, i.e., the absorber tubes, or the walls of the receiver tube itself. At each step, once it is determined which surface is hit by the ray, it must be decided if it is absorbed, transmitted, or reflected, comparing the optical coefficients to a random ρ

$$\begin{aligned} 0 \leq \rho \leq R_s, & \text{ reflection,} \\ R_s < \rho \leq R_s + T_s, & \text{ transmission,} \\ R_s + T_s < \rho \leq 1, & \text{ absorption,} \end{aligned} \quad (6)$$

where the subscript “s” indicates that the coefficients of the surface in question are considered. At the beginning of the propagation of each ray, a random number is generated and compared to the reflectivity of the outer wall of the receiver tube, to determine if the ray is reflected or enters the reaction space. In case the ray is reflected, its propagation is terminated, and a new ray is propagated; otherwise, the ray is considered to enter the reactor volume and its propagation

is continued. If at any point a ray is transmitted to the outside of the reactor, it is counted as lost and a new ray is generated. If it is reflected on an inner surface, the new propagation direction is obtained from the vector form of the law of reflection

$$\hat{\mathbf{r}} = \hat{\mathbf{i}} - 2(\hat{\mathbf{n}} \cdot \hat{\mathbf{i}})\hat{\mathbf{n}}, \quad (7)$$

where $\hat{\mathbf{r}}$, $\hat{\mathbf{i}}$, and $\hat{\mathbf{n}}$ are the reflected, incident, and normal unit vectors. After the new direction is obtained, the next intersection of the ray with a wall is sought.

On the other hand, if a ray is absorbed in an area element, a count is registered for this element, and a new ray is propagated. Typically, a million rays are propagated in each run. After all rays have been propagated, the radiative power absorbed at each surface element can be obtained by the following equation:

$$Q_{(i,j)} = \frac{P_{\text{ray}}}{A_{i,j}} \sum N_{i,j}, \quad (8)$$

where $A_{i,j}$ correspond to the area of the element (i, j) , $N_{i,j}$ is the number of rays absorbed, and P_{ray} is the power assigned to each ray or power per photon. The P_{ray} value is obtained as a function of the solar irradiance energy distribution, and the total number of rays impinging the receiver. The area elements are obtained by dividing the perimeter of each tube into equal angular segments. Each element spans the whole length of the tube (longitudinal symmetry of the problem is assumed) and the whole thickness of the film.

The analyzed quantities are the distribution of power absorbed in the perimeter of the tubes per unit area, the total power absorbed by each tube, and the yearly energy absorbed by each tube configuration.

2.3. Analyzed Cases. Traditionally, fixed thin film analysis considers only the amount of film catalyst deposited on the supported tubes as the design parameter of importance. The geometrical arrangement of the tubes is commonly chosen arbitrary or selected due to a simple symmetric disposition. In this work, six configurations are compared in order to obtain the most effective design. For the first scenario, a four-tube square configuration is studied (see Figure 5(a)). For a second scenario, a five-tube configuration in a pentagram disposition is analyzed (see Figure 5(b)). This disposition is the reference case, being the configuration initially built and tested by Salgado-Tránsito et al. [17] for the degradation of the pesticide carbaryl. The third scenario consists of six tubes, with a pentagram disposition similar to the second scenario, but with smaller diameter, and adds a center tube (Figure 5(c)). The fourth case preserves the number of the tubes from the latter, but it considers a displacement of the surrounding tubes away from the centered one, closed to the receiver tube (Figure 5(d)). The fifth scenario does the opposite, moving the surrounding tubes closer to the center (Figure 5(e)). Finally, the sixth case preserves the geometry of the third case but with a rotation of the whole tube configuration by $\pi/5$ (Figure 5(f)).

All configurations are compared considering the same solar irradiance conditions, as well as the same CPC design (concentration factor and tubular receiver diameter). It is worth noticing that the total catalyst film area available for absorption is kept constant between the different configurations, by suitable choice of the radius of the tubes. Moreover, the total mass of TiO_2 considered is the same in all cases as thickness is not varied either. The only variations lie in the number, radius, and angular disposition of the absorber tubes.

3. Results

In this section, results obtained from annual performance analysis are discussed. The absorption rate is calculated for every scenario, absorber tube arrangement, date, and hour. The absorption parameter $Q_{(i,j)}$ is integrated to obtain average absorption rates for every tube, as well as for every configuration as a whole.

Figure 6 shows the absorption rate for the outer wall of the 5 tubes of configuration 2, for the 21st of June, at 13:00 hours. Beam and diffuse radiation results are presented separately, to see the effect of the different angular composition of incident radiation; while beam radiation comes from a single direction (approximately 23° from the normal to the aperture, in the plane of the collector cross section), diffuse radiation comes from every possible direction on a hemisphere around the aperture normal. It can be seen that for beam solar radiation, the upper tubes (i.e., tubes 1, 2, and 3 of Figure 4(b)) have a higher absorption rate on the upper zones (from 0° to 180°), with a peak around 90° , while the bottom tubes (tubes 4 and 5) have a wider collection angle due to the intrinsic downside reflections of the CPC geometry (involute section). There is however, asymmetry, because radiation is coming more inclined towards tube 4, resulting in lateral reflections to this tube (180°), while tube 5 receives more radiation from the section of the involute closest to the receiver tube bottom. It is also noticeable that tube 2 and tube 3 have smaller absorption on its bottom part (from 200° to 320°) due to the effect of “shadowing” from the bottom tubes. A small amount that impinges tube 3 is due to lateral reflections of the CPC. These results are consistent with the distribution of incoming radiation at the walls of the reactor (receiver tube).

Meanwhile, for diffuse radiation, the situation is very different for each tube. Tube 1 receives radiation mainly from the right, tube 3 mainly from the left, and tube 2 (the top tube) both from left and right. The asymmetries observed are attributable to partial ground reflection of the diffuse component. The bottom tubes are illuminated from the bottom left and bottom right.

A similar analysis can be carried out for every configuration. In particular, Figure 7 compares results of configurations 2 and 3. In the latter, a sixth tube has been added at the center of the reaction space, and the diameter of the tubes has been decreased, to preserve the same total catalyst mass. For the 6-tube configuration, it is noticeable that although the tubes are smaller in comparison with the 5-tube case, the absorption rate for the external tubes remains almost

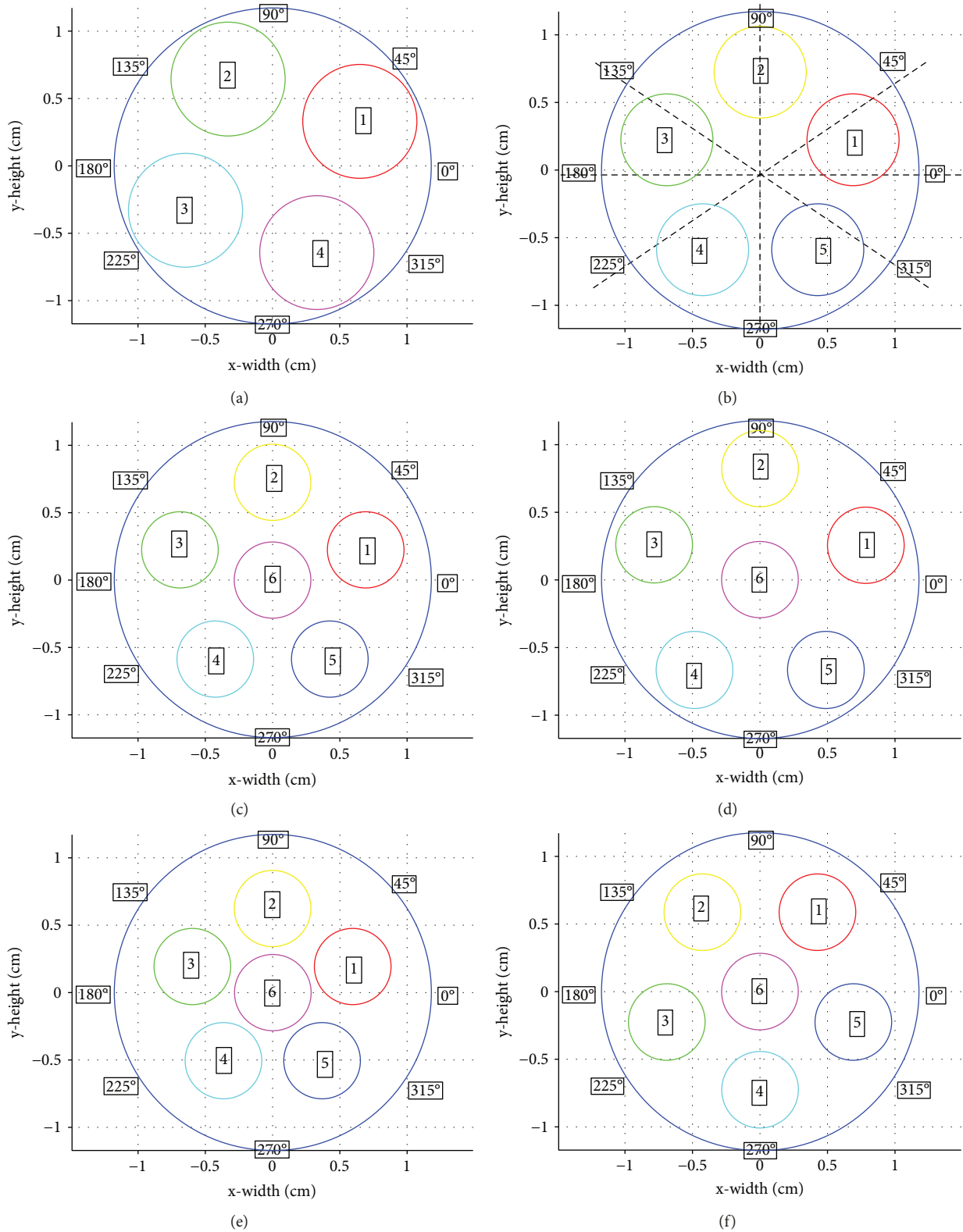


FIGURE 5: Diagram of the multitubular configurations analyzed: (a) four tubes in a square; (b) five tubes in pentagram disposition; (c) six tubes in a pentagram disposition with central tube; (d) six tubes with increased distance; (e) six tubes with decreased distance; (f) six tubes rotated by $\pi/5$.

the same. Due to the inclusion of a central tube (tube 6), the configuration is capable of capturing solar rays that pass along the spaces between the tubes in configuration 2 and

that were going to be lost through the receiver wall. Furthermore, the bottom tubes (4 and 5) are less “shadowed” by the upper tubes and capture a greater amount of photons in its

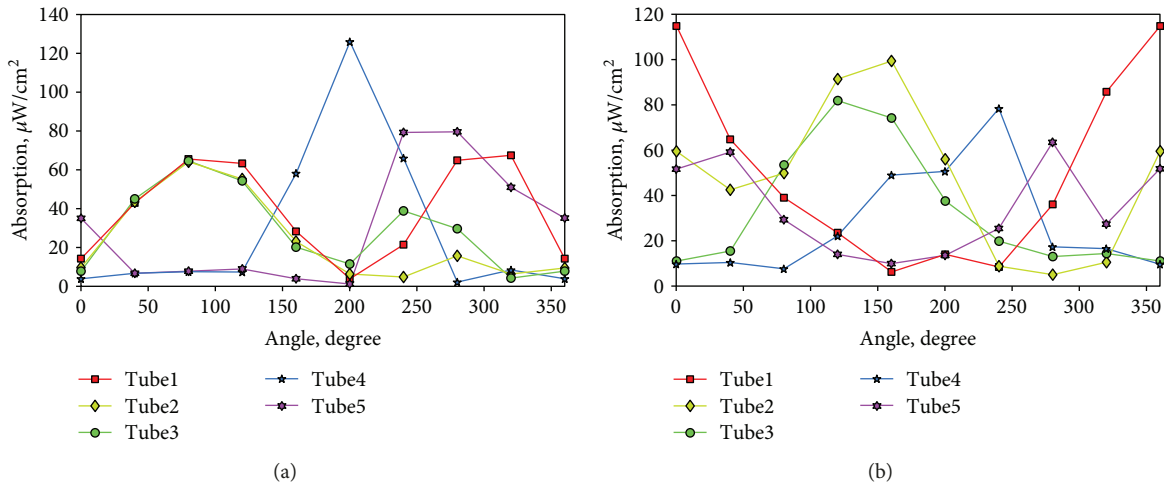


FIGURE 6: Power flux absorption distribution for the 5 tubes in configuration 2. June 21st at 13:00 hours. Beam (a) and diffuse (b) radiation contributions.

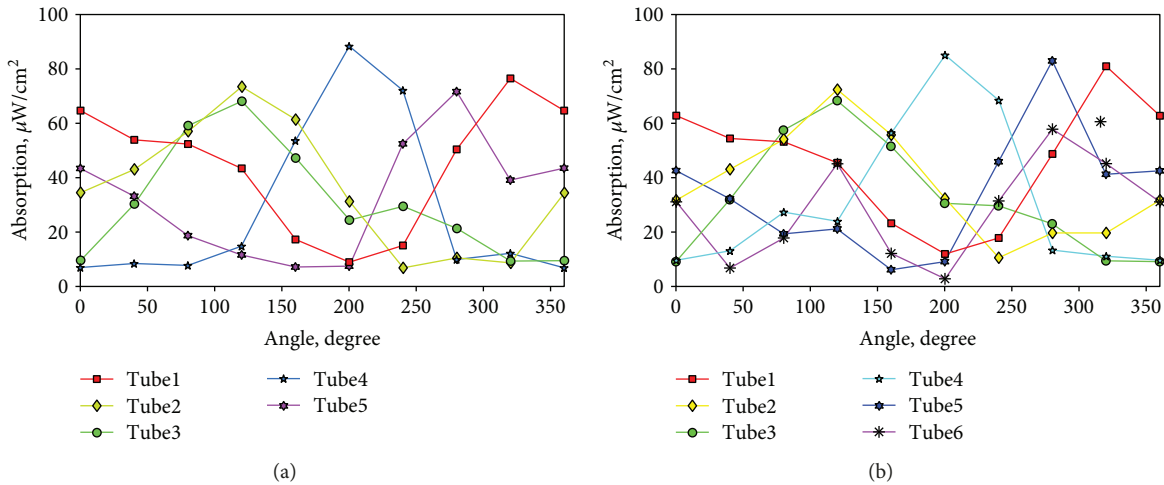


FIGURE 7: Power flux absorption distribution for the tubes in configurations 2 (a) and 3 (b), for combined beam and diffuse irradiance. June 21st at 13:00 hours.

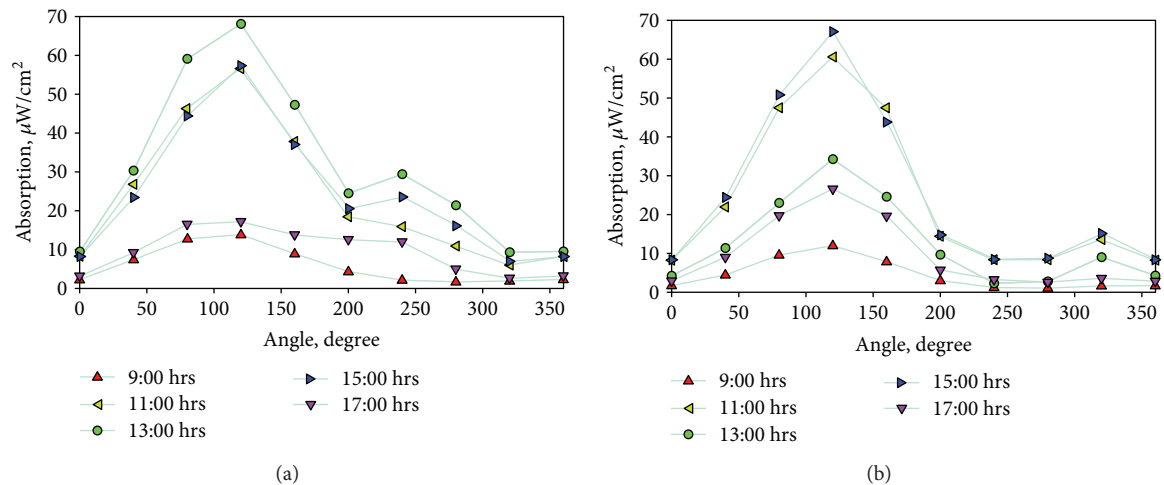


FIGURE 8: Power flux absorption distribution for tube 3, in configuration 2, for different hours. June 21st (left) and December 21st (right).

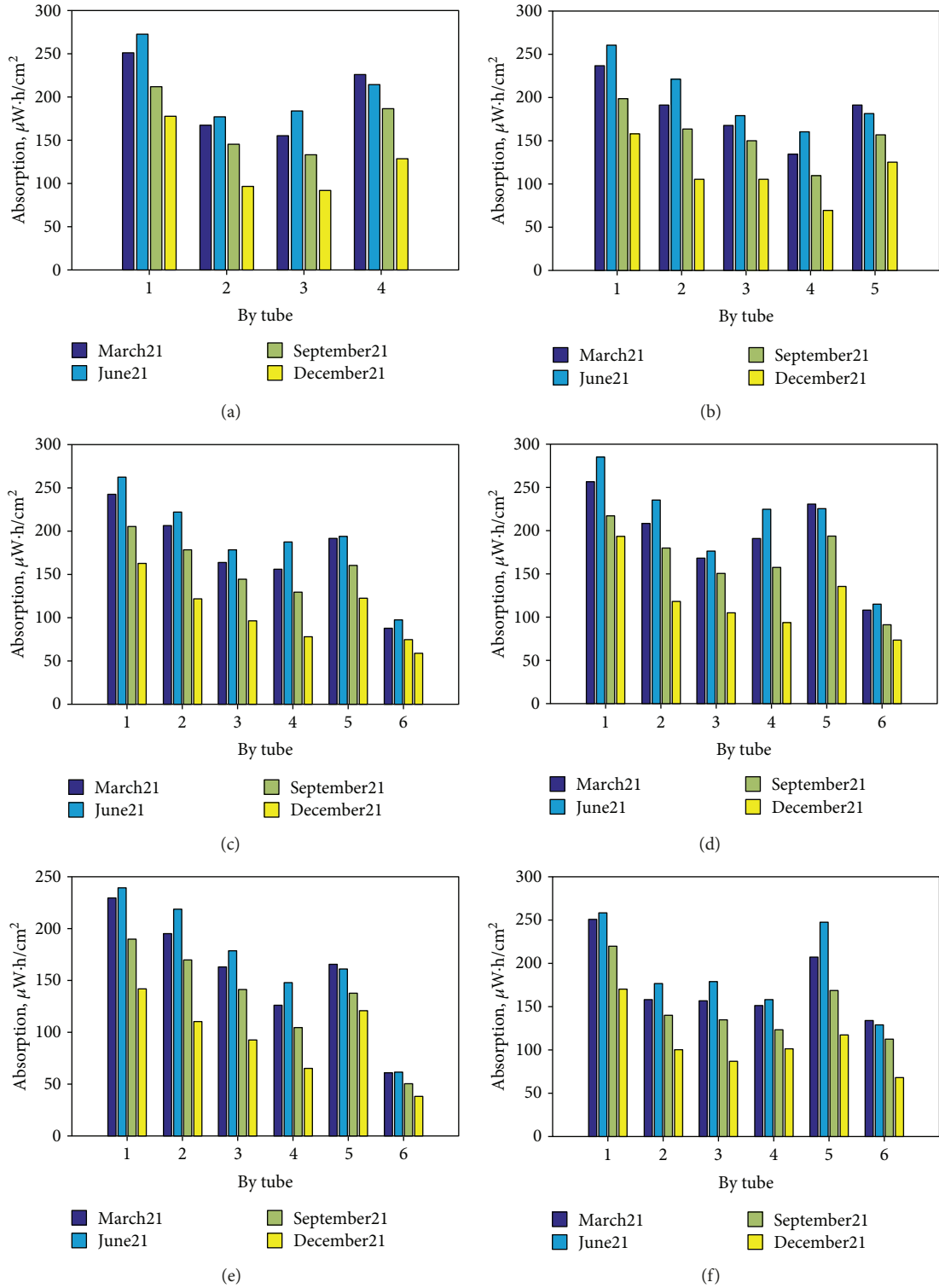


FIGURE 9: Average energy absorption for the solstices and equinoxes, for each tube in the different configurations. Panels (a) to (f) correspond to cases 1 to 6, respectively.

upper side (0° to 180°). Thus, an increase in performance is expected from the configurations with 6 tubes.

In Figure 8, the results are presented for different hours of the day for a single tube (tube 3), both for the 21st of June and the 21st of December, for combined beam and diffuse contributions. It is immediately clear that the absorption

distribution maintains the same shape during the day, changing only in height as the incident solar irradiance changes with the hour. Small variations in the morning and afternoon can be appreciated due to a steeper angle of sunlight entering the CPC aperture. The reason for this preserved shape of the curves along the day is that the angle of beam radiation keeps

more or less constant in the plane perpendicular to the receiver tube axis, because of the east-west orientation of this receiver. Thus, the angle changes occur mainly in the plane that contains the tube axis and the collector aperture normal, producing mainly a change in the collected power but not in the absorption distribution.

In both cases of Figure 7, the main contribution of absorbed radiation takes place at the top half of the tube. There is a secondary peak that displaces from the left bottom part of the tube for the summer and to the right bottom part for the winter. This is easy to understand, considering that the incidence angle to the normal of the collector is symmetrical for both dates, at 23.45° to the right and left, respectively.

For Figure 9, the flux absorption is averaged over the perimeter of each tube. The graph compares the average power absorption of each tube in each of the configurations, for the solstices and equinoxes, which are the more representative days of the year. The first feature that can be noted is the clear seasonal differences, attributable mainly to the variations on the duration of day along the year. Note however that the two equinoxes, that have the same sunlight duration, have very different absorbed power levels for different tubes. On the average, the power absorbed is less in September than in March, because autumn is the rainy season (see Figure 2). However, this is not true in every case, because the incident power in different tubes for different times of the year is also influenced by the distribution of incident rays on the tube walls.

Let us make a remark regarding units: if one wishes to compare the present results with those of Valadés-Pelayo et al. [7], it should be taken into account that the quantities presented are slightly different. In that paper, the power absorbed by the tubes was expressed in W/m^3 , which refers to the power absorbed by the catalyst film per unit volume. However, we have preferred here to express results in terms of energy absorbed per film outer surface area $\mu Wh/cm^2$. The rationale being that charge separation, recombination, and degradation reactions take place at the catalyst surface; hence, radiation absorption per unit surface, not per unit volume, is a measure that better represents the behavior of the reactor. However, both are valid manners of expressing the same physical situation.

Yearly mean absorbed power flux is used as comparison parameter between configurations in Figure 10. It is obtained by averaging the absorbed power flux of each tube over all working hours of the year. It can be noticed that the configuration that presents the greatest absorption rate through the year is case 4, the 6-tube-far configuration. This configuration preserves the advantages of using a central tube, but higher photon energy is captured by bringing the tubes closer to the external receiver, intercepting a greater fraction of the rays reflected by the CPC. The 6-tube-far configuration exceeds up to 30% in the performance absorption rate from the 4-tube configuration (case 1) and up to 13% more efficiency versus the 6-tube configuration 3.

Finally, in Table 1, the total energy absorbed over one year is presented for the different configurations. Clearly, configuration 4 is the winner, with 13% improvement with respect to the initially proposed geometry (configuration 2).

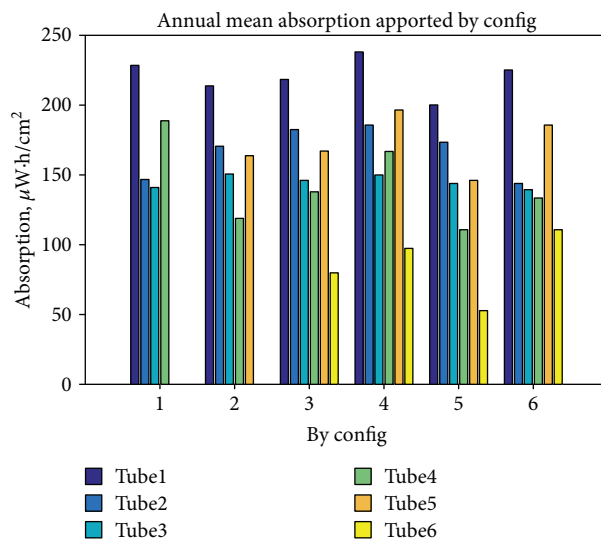


FIGURE 10: Comparison of energy absorption averaged over the whole year, for each tube of all the configurations. Config: 1 (Figure 9(a)); 2 (Figure 9(b)); 3 (Figure 9(c)); 4 (Figure 9(d)); 5 (Figure 9(e)); 6 (Figure 9(f)).

TABLE 1: Total annual absorbed energy for the different configurations.

Configuration	Annual absorbed energy (W·h)
(1) 4 tubes	48.4
(2) 5 tubes	44.8
(3) 6 tubes	47.0
(4) 6-tube-far	50.8
(5) 6-tube-near	43.1
(6) 6-tube-rot $\pi/5$	44.0

However, we can see that case 1 also shows a better performance. In both cases, this has to do with the reduction of losses through the tube gaps. However, from the point of view of better distribution of the catalyst over the reaction space, configuration 4 is clearly advantageous. The absorption by this improved configuration amounts approximately to 56% of the solar UV energy incident in the CPC collector during the entire year. This is quite a good performance, if we compare this with values typical of suspended catalyst reactors [19], where the limitations to absorption are imposed mainly by backscattering of radiation. In the present fixed catalyst configuration, reflection and transmission of radiation on the catalyst film produce also losses to the outside of the reactor.

4. Conclusions

In this study, the seasonal and yearly optical performance of CPC solar photocatalytic reactor with supported catalyst has been theoretically analyzed. A detailed model for the optical response of the anatase catalyst films has been utilized, together with Monte Carlo ray tracing simulations. The catalyst is supported over glass tubes contained inside a larger

glass tube that functions as receiver of the CPC reflector. Different configurations of catalyst support have been considered in terms of number and arrangement of the supporting tubes. Arrangements with four, five, and six tubes have been considered. The radius of the tubes is adjusted as their number increases, in order to have the same surface area in all compared cases. The case of five tubes, proposed in a previous work on semiempirical grounds, serves as a reference case for comparison. Important seasonal dependence of the response of the different tubes on each array is observed. Overall, the five-tube scenario presents the worst performance of all, followed by some of the 6-tube cases, because they leave free trajectories for solar rays to cross the reactor. In general, the six-tube configurations are better than the originally proposed, but nevertheless important differences can be observed depending on the specific arrangement of tubes. Another interesting result is that the six-tube case and the rotated six-tube case present almost the same absorption capacity, proving that symmetrical rotations have very little effect on global performance. As can be seen, the six-tube case surpasses the absorption rate of all the other configurations in every working day of the year when the distance between tubes is extended to cover a larger cross section. This configuration exhibits 13% increased yearly energy absorption with respect to the reference. As a main conclusion, it can be said that the development of a modeling tool for evaluating rigorously the annual performance optical of CPC's photocatalytic reactors provides valuable insights to improve the design of the system.

Data Availability

No data were used to support this study.

Conflicts of Interest

The authors declare that they have no conflicts of interest.

Acknowledgments

The authors acknowledge CONACYT for the financial support for the project Problemas Nacionales 2015-01-1651: "Diseño y Construcción de Potabilizador Integral Solar de Agua para Comunidades Rurales". The authors also acknowledge the support from Fondo Sectorial CONACYT-SENER-Sustentabilidad Energetica through Grant 207450 and Centro Mexicano de Innovación en Energía Solar (CeMIE-Sol), within strategic project no. 10, "Combustibles Solares y Procesos Industriales" (COSOLPi). Patricio Valades-Pelayo also acknowledges a postdoctoral fellowship by DGAPA-UNAM and a "Retención" scholarship by CONACYT.

References

- [1] C. S. Lugo-Vega, B. Serrano-Rosales, and H. de Lasa, "Immobilized particle coating for optimum photon and TiO₂ utilization in scaled air treatment photo reactors," *Applied Catalysis B: Environmental*, vol. 198, pp. 211–223, 2016.
- [2] A. Pinedo, M. López, E. Leyva, B. Zermeño, B. Serrano, and E. Moctezuma, "Photocatalytic decomposition of metoprolol and its intermediate organic reaction products: kinetics and degradation pathway," *International Journal of Chemical Reactor Engineering*, vol. 14, no. 3, pp. 809–820, 2016.
- [3] S. Escobedo, B. Serrano, A. Calzada, J. Moreira, and H. de Lasa, "Hydrogen production using a platinum modified TiO₂ photocatalyst and an organic scavenger. Kinetic modeling," *Fuel*, vol. 181, pp. 438–449, 2016.
- [4] U. J. Rajput, H. Alhadrami, F. al-Hazmi, Q. Guo, and J. Yang, "Initial investigations of a combined photo-assisted water cleaner and thermal collector," *Renewable Energy*, vol. 113, pp. 235–247, 2017.
- [5] K. Nakata and A. Fujishima, "TiO₂ photocatalysis: design and applications," *Journal of Photochemistry and Photobiology C: Photochemistry Reviews*, vol. 13, no. 3, pp. 169–189, 2012.
- [6] J. Marugán, R. van Grieken, A. E. Cassano, and O. M. Alfano, "Quantum efficiency of cyanide photooxidation with TiO₂/SiO₂ catalysts: multivariate analysis by experimental design," *Catalysis Today*, vol. 129, no. 1-2, pp. 143–151, 2007.
- [7] P. J. Valadés-Pelayo, C. A. Arancibia-Bulnes, I. Salgado-Tránsito, H. I. Villafán-Vidales, M. I. Peña-Cruz, and A. E. Jiménez-González, "Effect of photocatalyst film geometry on radiation absorption in a solar reactor, a multiscale approach," *Chemical Engineering Science*, vol. 161, pp. 24–35, 2017.
- [8] V. Loddo, S. Yurdakal, G. Palmisano et al., "Selective photocatalytic oxidation of 4-methoxybenzyl alcohol to p-anisaldehyde in organic-free water in a continuous annular fixed bed reactor," *International Journal of Chemical Reactor Engineering*, vol. 5, no. 1, 2007.
- [9] G. E. Imoberdorf, G. Vella, A. Sclafani, L. Rizzuti, O. M. Alfano, and A. E. Cassano, "Radiation model of a TiO₂-coated, quartz wool, packed-bed photocatalytic reactor," *AIChE Journal*, vol. 56, no. 4, pp. 1030–1044, 2010.
- [10] G. E. Imoberdorf, F. Taghipour, M. Keshmiri, and M. Mohseni, "Predictive radiation field modeling for fluidized bed photocatalytic reactors," *Chemical Engineering Science*, vol. 63, no. 16, pp. 4228–4238, 2008.
- [11] S. Malato, J. Blanco, D. C. Alarcón, M. I. Maldonado, P. Fernández-Ibáñez, and W. Gernjak, "Photocatalytic decontamination and disinfection of water with solar collectors," *Catalysis Today*, vol. 122, no. 1-2, pp. 137–149, 2007.
- [12] E. R. Bandala, C. A. Arancibia-Bulnes, S. L. Orozco, and C. A. Estrada, "Solar photoreactors comparison based on oxalic acid photocatalytic degradation," *Solar Energy*, vol. 77, no. 5, pp. 503–512, 2004.
- [13] C. A. Arancibia-Bulnes and S. A. Cuevas, "Modeling of the radiation field in a parabolic trough solar photocatalytic reactor," *Solar Energy*, vol. 76, no. 5, pp. 615–622, 2004.
- [14] J. Blanco, S. Malato, P. Fernández et al., "Compound parabolic concentrator technology development to commercial solar detoxification applications," *Solar Energy*, vol. 67, no. 4-6, pp. 317–330, 1999.
- [15] J. Colina-Márquez, F. Machuca-Martínez, and G. Li Puma, "Photocatalytic mineralization of commercial herbicides in a pilot-scale solar CPC reactor: photoreactor modeling and reaction kinetics constants independent of radiation field," *Environmental Science and Technology*, vol. 43, no. 23, pp. 8953–8960, 2009.
- [16] S. Malato Rodríguez, J. Blanco Gálvez, M. I. Maldonado Rubio et al., "Engineering of solar photocatalytic collectors," *Solar Energy*, vol. 77, no. 5, pp. 513–524, 2004.

- [17] I. Salgado-Tránsito, A. E. Jiménez-González, M. L. Ramón-García, C. A. Pineda-Arellano, and C. A. Estrada-Gasca, "Design of a novel CPC collector for the photodegradation of carbaryl pesticides as a function of the solar concentration ratio," *Solar Energy*, vol. 115, no. 0, pp. 537–551, 2015.
- [18] J. Chaves and M. C. Pereira, "New CPC solar collector for planar absorbers immersed in dielectrics. Application to the treatment of contaminated water," *Journal of Solar Energy Engineering*, vol. 129, no. 1, pp. 16–21, 2007.
- [19] C. A. Arancibia-Bulnes, E. R. Bandala, and C. A. Estrada, "Radiation absorption and rate constants for carbaryl photocatalytic degradation in a solar collector," *Catalysis Today*, vol. 76, no. 2-4, pp. 149–159, 2002.
- [20] J. Colina-Márquez, F. Machuca-Martínez, and G. L. Puma, "Radiation absorption and optimization of solar photocatalytic reactors for environmental applications," *Environmental Science & Technology*, vol. 44, no. 13, pp. 5112–5120, 2010.
- [21] A. Manassero, M. L. Satuf, and O. M. Alfano, "Photocatalytic reactors with suspended and immobilized TiO₂: comparative efficiency evaluation," *Chemical Engineering Journal*, vol. 326, pp. 29–36, 2017.
- [22] M. Born and E. Wolf, *Principles of Optics: Electromagnetic Theory of Propagation, Interference and Diffraction of Light*, Cambridge University Press, 1999.
- [23] M. Blanco, A. Mutuberria, A. Monreal, and R. Albert, "Results of the empirical validation of Tonatiuh at Mini-Pegase CNRS-PROMES facility," in *SolarPACES 2011 Granada*, Spain, 2011.
- [24] J. A. Duffie and W. A. Beckman, *Solar Engineering of Thermal Processes 4th Edition*, Wiley, 2013.
- [25] M. Rubin, "Optical properties of soda lime silica glasses," *Solar Energy Materials*, vol. 12, no. 4, pp. 275–288, 1985.



Hindawi

Submit your manuscripts at
www.hindawi.com

